Temporal and spatial manipulation of the recolliding wave packet in strong-field photoelectron holography

Mingrui He,[1] Yang Li,[1] Yueming Zhou,[1,*] Min Li,[1] and Peixiang Lu[1,2,†]
[1]*School of Physics, Huazhong University of Science and Technology, Wuhan 430074, China*
[2]*Laboratory of Optical Information Technology, Wuhan Institute of Technology, Wuhan 430205, China*
(Received 19 November 2015; published 7 March 2016)

We theoretically demonstrate temporal and spatial manipulation of electron wave packets involved in strong-field photoelectron holography (SFPH) with the orthogonally polarized two-color laser fields. By varying the relative phase of the two-color fields, the recollision time of the returning wave packet can be accurately controlled, which allows us to switch off and on the holographic interference. Moreover, the recollision angles of the returning electron wave packet can be arbitrarily controlled via changing the relative intensity of the two-color fields, and thus the structure information of the target is encoded in the hologram by the recollision electron wave packet from different angles. This makes the SFPH a powerful technique of imaging the molecular structure as well as ultrafast dynamics on an attosecond time scale.

DOI: 10.1103/PhysRevA.93.033406

I. INTRODUCTION

Tunneling ionization of the atoms and molecules exposed to a strong laser field is a fundamental process in intense laser-matter interactions and it is the basis for other strong-field processes [1–8]. During a laser pulse, there are different pathways for the tunneling ionized electrons to achieve the same final momentum. Due to the coherent nature of these tunneled electron wave packets (EWPs), interference patterns appear in the final photoelectron momentum distributions (PMDs). Generally, the interference patterns can be classified into two categories, intercycle and intracycle interferences. The intercycle interference arises from EWPs released periodically in time at subsequent laser cycles, which results in the well-known above-threshold ionization (ATI) peaks [9]. For the intracycle interference, the EWPs launched within one cycle at times where the vector potential is the same but the direction of the electric field is opposite [10,11]. This interference is presented as the modulation of the ATI peaks in PMDs [12]. It has been shown that this interference pattern in PMDs could provide deep insight into the electronic structure of atoms and molecules and the attosecond electronic dynamics during the tunneling ionization process [13].

After tunneling ionization, the electron is accelerated in the oscillating laser field and may rescatter off the parent ion when it is driven back [14]. The rescattered electrons could have the same final momentum as the electrons that reach the detector directly after tunneling ionization, giving rise to another important interference referred to as strong-field photoelectron holography (SFPH) [15,16], by analogy to the optical holography [17]. In SFPH, the tunneled electron wave packet that reaches the detector without further interaction with the parent ion acts as the reference wave and the rescattered electron wave packet plays as the signal wave. Recently, this holographic interference has been experimentally observed for different targets [15,18–20]. Because of the rescattering, the spatial and temporal information of the parent ion and electron dynamics of the tunneling process are stored in and can be retrieved from the hologram. For example, the distance between the electron and ion at tunneling has been experimentally extracted [18] and the phase structure of the continuum EWP at tunneling was also revealed by analyzing the holographic interference patterns [19]. Very recently, it has been theoretically demonstrated that a fundamental quantity, the phase of the scattering amplitude, could be extracted from the holographic interference patterns [21].

Usually, all of these interferences contribute together to the final PMDs and thus the interference patterns in PMDs are too complicated for people to extract useful information. So it is necessary to select some certain interferences to extract information. Here, we demonstrate the selection of the holographic interference by temporally and spatially manipulating the involved electron wave packets with orthogonally polarized two-color (OTC) fields [22]. Recent studies have shown that the OTC field is an efficient tool to control electron dynamics in strong-field processes. For example, it has been employed to generate high-order harmonics with very large ellipticity [23] and to select their long and short orbits [24]. By analyzing the high-order harmonics spectra in the OTC fields, the time when an electron exits the tunneling barrier was accurately resolved [25,26] and the atomic wave functions [27] as well as molecular orbits [28] are successfully probed. The OTC fields have also been used to control the electron correlations in strong-field nonsequential double ionization [29–31]. Recently, it has been demonstrated that the OTC fields can disentangle the intracycle and intercycle interferences of the tunneled electron wave packets [32–34]. In this paper, we show that by varying the relative phase of the OTC fields, the recollision time of the returning electron wave packet can be accurately controlled and thus we can selectively switch off and on the holographic interference. Additionally, the recollision angle of the returning electron wave packet can be adjusted by the relative intensity of the OTC fields, enabling SFPH to record the structure of the target with recollision electrons from different recollision angles. This is of special importance for imaging molecular structure and ultrafast dynamics with the scheme of SFPH.

*zhouymhust@hust.edu.cn
†lupeixiang@hust.edu.cn

II. NUMERICAL METHODS

A. Full quantum simulation

To investigate the ionization of atoms induced by OTC fields, we numerically solve the two-dimensional time-dependent Schrödinger equation (2 D-TDSE) with the single-active-electron (SAE) approximation. The TDSE reads [atomic units (a.u.) are used throughout unless stated otherwise]

$$i\frac{\partial}{\partial t}\Psi(\vec{r},t) = \mathcal{H}(\vec{r},t)\Psi(\vec{r},t), \tag{1}$$

where $\vec{r} = (x,y)$ denotes the electron position in the polarization plane of the OTC fields. In length gauge, the Hamiltonian $\mathcal{H}(\vec{r},t)$ is given by

$$\mathcal{H}(\vec{r},t) = -\tfrac{1}{2}\nabla^2 + V(r) + \vec{r}\cdot\vec{E}(t). \tag{2}$$

We choose argon as the target atom. $V(r)$ is the effective soft-core potential:

$$V(r) = -\frac{1}{\sqrt{x^2+y^2+a}}. \tag{3}$$

The soft-core parameter a is set to be 0.39 to correctly reproduce the ground-state energy of the argon atom. The electric field $\vec{E}(t)$ of the OTC pulses is defined as

$$\vec{E}(t) = f(t)\left[E_x\cos(\omega t)\vec{x} + E_y\cos\left(\tfrac{1}{2}\omega t + \phi\right)\vec{y}\right]. \tag{4}$$

Here, $f(t)$ is the pulse envelope which has a $\sin^2(\pi t/T_p)$ form with a duration of $T_p = 8T$. (T is the optical cycle period of the 800-nm pulse.) $\omega = 0.057$ a.u. is the angular frequency of the 800-nm pulse. The intensity of the 800-nm laser field (polarized along the x axis) I_x is fixed at 1.5×10^{14} W/cm^2, while I_y, the intensity of the 1600-nm laser pulse (polarized along the y axis) is tunable. E_x and E_y are the amplitudes of the 800-nm and 1600-nm components, respectively, and ϕ is the relative phase of the two fields.

The split-operator spectral method [35] on a Cartesian grid is used to numerically solve the 2D-TDSE. The initial wave function is prepared by imaginary-time propagation [36]. Due to the linearity of the Schrödinger equation, for real-time propagation we split the electron wave function $\Psi(\tau)$ at any given time τ into two parts [37]:

$$\begin{aligned}\Psi(\tau) &= \Psi(\tau)[1 - F_s(R_c)] + \Psi(\tau)F_s(R_c)\\ &= \Psi_I(\tau) + \Psi_{II}(\tau).\end{aligned} \tag{5}$$

Here, $F_s(R_c) = 1/(1+e^{-(r-R_c)/\triangle})$ is an absorbing function [38] that separates the propagation space into the inner (0–R_c) and outer (R_c–$R_{\max}$) regions smoothly. $\Psi_I(\tau)$ propagates under the full Hamiltonian in the inner space, while $\Psi_{II}(\tau)$ represents the "ionized part" that propagates under the Volkov Hamiltonian in the outer space analytically [37,39]. More specifically, at the end of each time step the ionized wave packet $\Psi_{II}(\tau)$ is first transformed into momentum space,

$$C(\vec{p},\tau) = \int \Psi_{II}(\tau)\frac{e^{-i[\vec{p}+\vec{A}(\tau)]\cdot\vec{r}}}{2\pi}d^2\vec{r}, \tag{6}$$

where $\vec{A}(\tau) = -\int_0^\tau \vec{E}(\tau')d\tau'$ is the vector potential of the OTC fields. Then, we propagate the $\Psi_{II}(\tau)$ from time τ to the end of the laser pulse, using

$$\Psi(\infty,\tau) = \int \bar{C}(\vec{p},\tau)\frac{e^{-i\vec{p}\cdot\vec{r}}}{2\pi}d^2\vec{p}, \tag{7}$$

with $\bar{C}(\vec{p},\tau) = e^{-i\int_\tau^\infty \frac{1}{2}[\vec{p}+\vec{A}(\tau')]^2 d\tau'}C(\vec{p},\tau)$. Finally, we obtain the PMD by the relation

$$\frac{dP(\vec{p})}{dEd\theta} = \left|\sum_\tau \bar{C}(\vec{p},\tau)\right|^2. \tag{8}$$

Here, $E = |\vec{p}|^2/2$ is the electron energy and θ is the angle of the emitted electron. In our simulation, the time step of propagation is $\triangle t = 0.1$ a.u. At the end of the pulse, the wave function is propagated for an additional few femtoseconds to collect "slow" electrons [40]. The Cartesian grid ranges from -819 a.u. to 819 a.u. for both directions with a grid size of $\triangle x = \triangle y = 0.1$ a.u. The boundary of the inner space is $R_c = 180$ a.u. with $\Delta = 8$ a.u..

B. Semiclassical simulation

Although the TDSE results could correctly produce the interference patterns in PMD, the physical origins of these interferences are missing. In what follows, we will introduce the generalized strong-field approximation (gSFA) model [41] to identify different interference patterns in PMDs. As done in the standard SFA [1,42,43], the strong-field ionization process is described by the following transition amplitude from the initial ground state ψ_i with binding energy of $-I_p$ to the final continuum state $\psi_{\vec{p}}$ with asymptotic momentum $\vec{p}$,

$$M_{\vec{p}i} = M^D_{\vec{p}i} + M^R_{\vec{p}i}, \tag{9}$$

where

$$M^D_{\vec{p}i} = -i\int_0^t dt'\langle\vec{p}+\vec{A}(t')|\vec{E}(t')\cdot\vec{r}|\psi_i\rangle e^{-iS_D} \tag{10}$$

is the direct part of the transition amplitude with

$$S_D = \frac{1}{2}\int_{t'}^t d\tau[\vec{p}+\vec{A}(\tau)]^2 - I_p t', \tag{11}$$

and

$$\begin{aligned}M^R_{\vec{p}i} = -\int_0^t dt'\int_{t'}^t dt''\langle\vec{p}+\vec{A}(t'')|V(\vec{r})|\vec{k}+\vec{A}(t'')\rangle\\ \times\langle\vec{k}+\vec{A}(t')|\vec{E}(t')\cdot\vec{r}|\psi_i\rangle e^{-iS_R}\end{aligned} \tag{12}$$

corresponds to the rescattered part with

$$\begin{aligned}S_R = \frac{1}{2}\int_{t'}^{t_r} d\tau[\vec{k}+\vec{A}(\tau)]^2\\ +\frac{1}{2}\int_{t_r}^t d\tau[\vec{p}+\vec{A}(\tau)]^2 - I_p t'.\end{aligned} \tag{13}$$

In the above equations, $\vec{A}(t) = -\int_0^t dt'\vec{E}(t')$ is the vector potential of the OTC laser fields. The calculation of the transition amplitude involves a five-dimensional integral over the ionization times, the intermediate momentum $\vec{k}$, and the rescattering times to evaluate, which numerically is not an easy task. Alternatively, the formulation of Feynman's path integral approach can be applied using the saddle-point method

[44]. The saddle points are the stationary points of Eqs. (11) and (13), which can be found by differentiating the action with respect to the integration variables, i.e., the ionization times, the intermediate momentum, and the rescattering times. For direct electrons, it simply involves ionization time t_i, yielding

$$\tfrac{1}{2}[\vec{p}+\vec{A}(t_i)]^2+I_p=0. \tag{14}$$

Equation (14) stands for the energy conservation law at the instant of ionization. Generally, the ionization times (t_i) associating with the relevant electron trajectories are all complex variables due to the tunneling nature of the ionization processes. These complex trajectories are also referred as quantum orbits [45,46]. Similarly, the saddle equations for rescattered electrons are expressed as

$$\frac{1}{2}[\vec{k}_s+\vec{A}(t_i)]^2+I_p=0, \tag{15}$$

$$\vec{k}_s=-\frac{1}{t_r-t_i}\int_{t_i}^{t_r}d\tau\vec{A}(\tau), \tag{16}$$

$$\frac{1}{2}[\vec{k}_s+\vec{A}(t_r)]^2=\frac{1}{2}[\vec{p}+\vec{A}(t_r)]^2, \tag{17}$$

where $\vec{k}_s$ is the stationary intermediate momentum and $\vec{p}$ is the final momentum of the electron. t_r is the recollision time of the rescattered electron. Equation (16) presents the return condition for the electron. Equations (15) and (17) stand for the energy conservation at the moment of ionization and rescattering. Since we focus on the SFPH originating from the interference between near-forward-scattering electrons and direct electrons, only the solutions with scattering angle less than 90° are taken into account. By numerically solving Eqs. (15)–(17) and selecting the corresponding solutions, the near-forward-scattering saddle points can be found. We would emphasize that in the saddle-point equations the two components of the OTC laser fields are treated equally without any additional assumptions. Inserting the saddle points into the direct and rescattering part of the transition amplitude, Eqs. (10) and (12) become

$$M_{\vec{p}i}^{D}=\sum_s \mathcal{C}(\vec{p},t_{is})e^{-iS_D(t_{is})} \tag{18}$$

and

$$M_{\vec{p}i}^{R}=\sum_s \mathcal{C}'(\vec{p},\vec{k}_s,t_{is},t_{rs})e^{-iS_R(\vec{k}_s,t_{is},t_{rs})}, \tag{19}$$

where $\mathcal{C}(\vec{p},t_{is})$ and $\mathcal{C}'(\vec{p},\vec{k}_s,t_{is},t_{rs})$ include all the pre-exponential terms [42]. So far, the gSFA method with the saddle-point approximation in the OTC laser fields is introduced. In the next section we will use it to identify different types of trajectories leading to the interference patterns in the PMD.

III. RESULTS AND DISCUSSION

The OTC pulses are shown in Fig. 1. We first use a strong 800-nm laser pulse with intensity of 1.5×10^{14} W/cm^2 and a weaker 1600-nm pulse with intensity 1/16 of the former. Under this condition, the tunneling of the EWPs is mainly caused by the 800-nm pulse, while the 1600-nm pulse only streaks the EWPs in the orthogonal direction. By adjusting

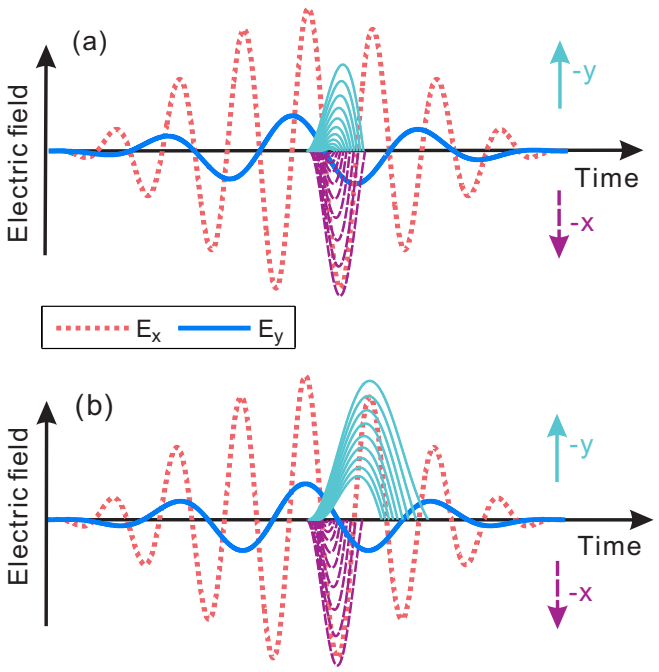

FIG. 1. Electron trajectories in OTC fields with relative phases of (a) $\phi=0.25\pi$ and (b) $\phi=0$. The 800-nm pulse (dotted red curve) is polarized along the x axis with an intensity of 1.5×10^{14} W/cm^2, and the 1600-nm pulse [dark blue curve] is polarized along the y axis with an intensity of 1/16 of the 800-nm field. For the sake of convenience, the two orthogonal components are drawn parallel for better visualization. Dashed purple and shallow blue curves, respectively, show x and y components of the sample trajectories, starting within the falling edge of the field. The colored arrows indicate the corresponding direction of the motions.

the relative phase between the two colors, we can manipulate the electron trajectories such that the electron can recollide with the parent ion or not. As shown in Fig. 1(a), we take the electrons liberated at the falling edge of the field as examples. For relative phase $\phi=0.25\pi$, the electron motions in the y direction correspond to the so-called short trajectories [14]; their recollision time is coincided with that of the x direction. Thus the recollision condition is satisfied and we could expect the SFPH to occur. Alternatively, the phase between the two colors can be chosen such that the long trajectories dominate in the y direction, as presented in Fig. 1(b) for $\phi=0$. In this case, the excursion time in the y direction is much longer than that in the x direction, making the electron miss the core. As a result, the SFPH will be switched off. Thus, by adjusting the phase delay of the two colors, we can make the electron recollide or miss the core, switching on and off the SFPH. In order to achieve this goal, the mid-infrared 1600-nm streaking field is adopted, which is much better than the 400-nm pulse in our case.

In the subsequent discussion, we focus on the PMDs induced by OTC fields with different relative phases. Figures 2(a) and 2(b) are the OTC laser fields used in the calculations, where the relative phases are $\phi=0.25\pi$ and $\phi=0$, respectively. Figures 2(c) and 2(d) present the corresponding PMDs calculated by TDSE. The distinct difference is that the SFPH pattern appears for $\phi=0.25\pi$ and disappears for

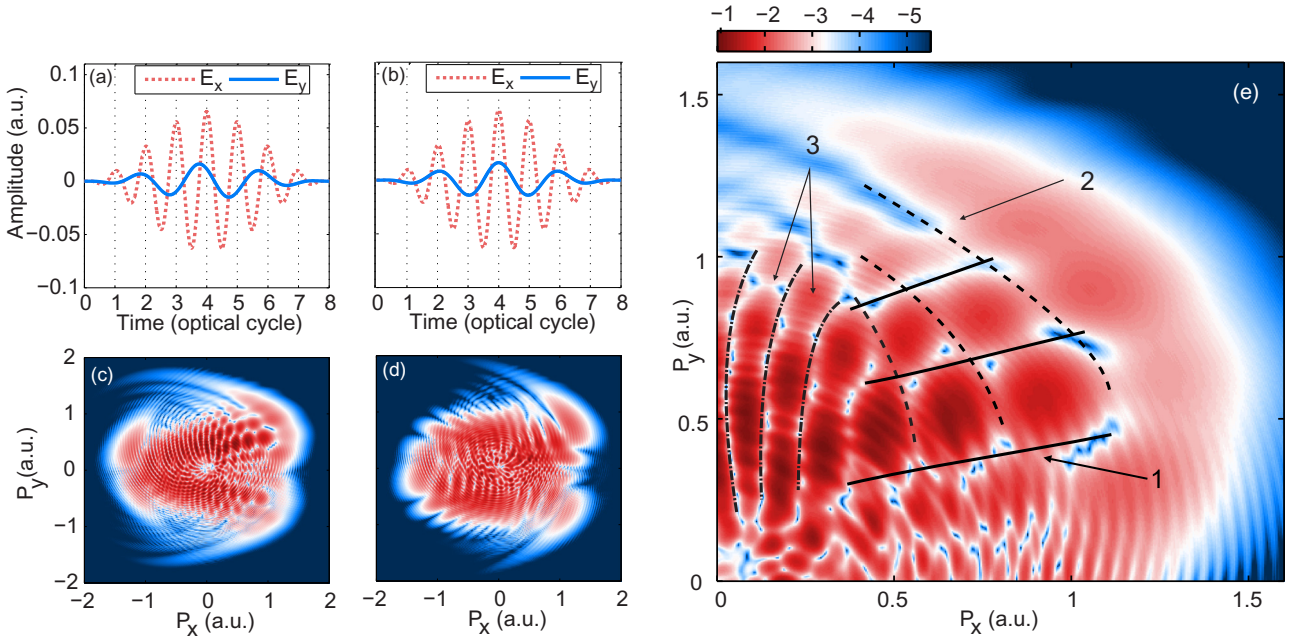

FIG. 2. Electric fields [(a) and (b)] and corresponding photoelectron momentum distributions [(c) and (d)]. The laser parameters are the same as Fig. 1. The relative phases are 0.25π in (a), (c) and 0 in (b), (d). (e) Enlarges the fist quadrant of (c) to highlight the different interference patterns marked as 1, 2, 3.

$\phi = 0$, which indicates that the OTC pulses offer subcycle control of the ionization dynamics. Additionally, in Fig. 2(c), the holographic interference is streaked by the 1600-nm pulse in the y direction, and thus two branches of the hologram appear in the first and forth quadrants, respectively. Besides the holographic patterns, there are other interference structures which can be identified from Fig. 2(c). For better visualization, Fig. 2(e) presents an enlarged view of the first quadrant of Fig. 2(c). As can be seen, three evident interference structures appear. The forklike pattern (marked as 1) is the holographic pattern [15]. The second interference (marked as 2) has an outcoming arc structure. The third interference (marked as 3) that has an incoming arc structure is identified as the intracycle interference, which also disappears when the relative phase changes to 0 [in Fig. 2(d)]. Switching on and off the intracycle interference by the OTC fields has been experimentally demonstrated and analyzed in Ref. [32].

In the following, the three distinct interference structures 1–3 in Fig. 2(e) are analyzed using the gSFA method. The results are shown in Fig. 3. To identify the origin of the interference patterns, we analyze two interfering waves with same final momentum (marked A and B in the figure). Their ionization times and paths are presented in the upper and middle row in Fig. 3, respectively. The bottom row of Fig. 3 is the interference patterns calculated by gSFA, where the pre-exponential terms in the transition amplitudes are omitted because their calculations for low-angle scattering meet serious difficulties: a divergence for near-forward scattering and therefore a highly overestimated magnitude for low angles. However, the pre-exponential terms only influence the contrast of the interference patterns. In Fig. 3(a), the near-forward-scattering electron (A) and the direct electron (B) are liberated in the same quarter cycle and start their motions on the same side of the parent ion, forming the forklike holographic pattern shown in the bottom row. While in Fig. 3(b), two electron wave packets A and B are liberated in adjacent quarter cycles and start their motions on the opposite sides of the ion, resulting in the near-semiring structure with an outcoming form. Besides the interferences of recollision and direct electrons, the intracycle interference formed by direct electrons (A and B) is analyzed in Fig. 3(c). The direct electrons are ionized in adjacent quarter cycles and start their paths on the opposite sides of the ion. Using the gSFA method, we provide a physical interpretation of different kinds of interferences in Fig. 2(e). At this stage, we have demonstrated switching on and off of the hologram by altering the relative phase ϕ.

As we mentioned above, the strong-field photoelectron holography is a potential tool to image atomic and molecular structures [21]. Due to the nonspherical symmetry of molecules, we should manipulate the recollision electron to recollide the molecules with different angles to get complete structural information. In linearly polarized laser fields, this could be realized by molecular alignment. Here we will show that the recollision angle of the returning electron wave packet could be manipulated by altering the intensity ratio of the OTC fields. In Fig. 4, the PMDs obtained by the 2D-TDSE are presented in the upper row. From columns (a)–(d), the relative laser intensity ratio $\varepsilon = I_y/I_x$ increases from 1/36 to 1. As can be seen in the PMDs, with the increasing I_y, the two branches of the hologram split out gradually in the orthogonal direction, implying the increasing recollision angle.

To present the recollision angles more intuitively, the paths of the near-forward-scattering electrons corresponding to the first quadrant of the PMDs in the upper row (in Fig. 4) are

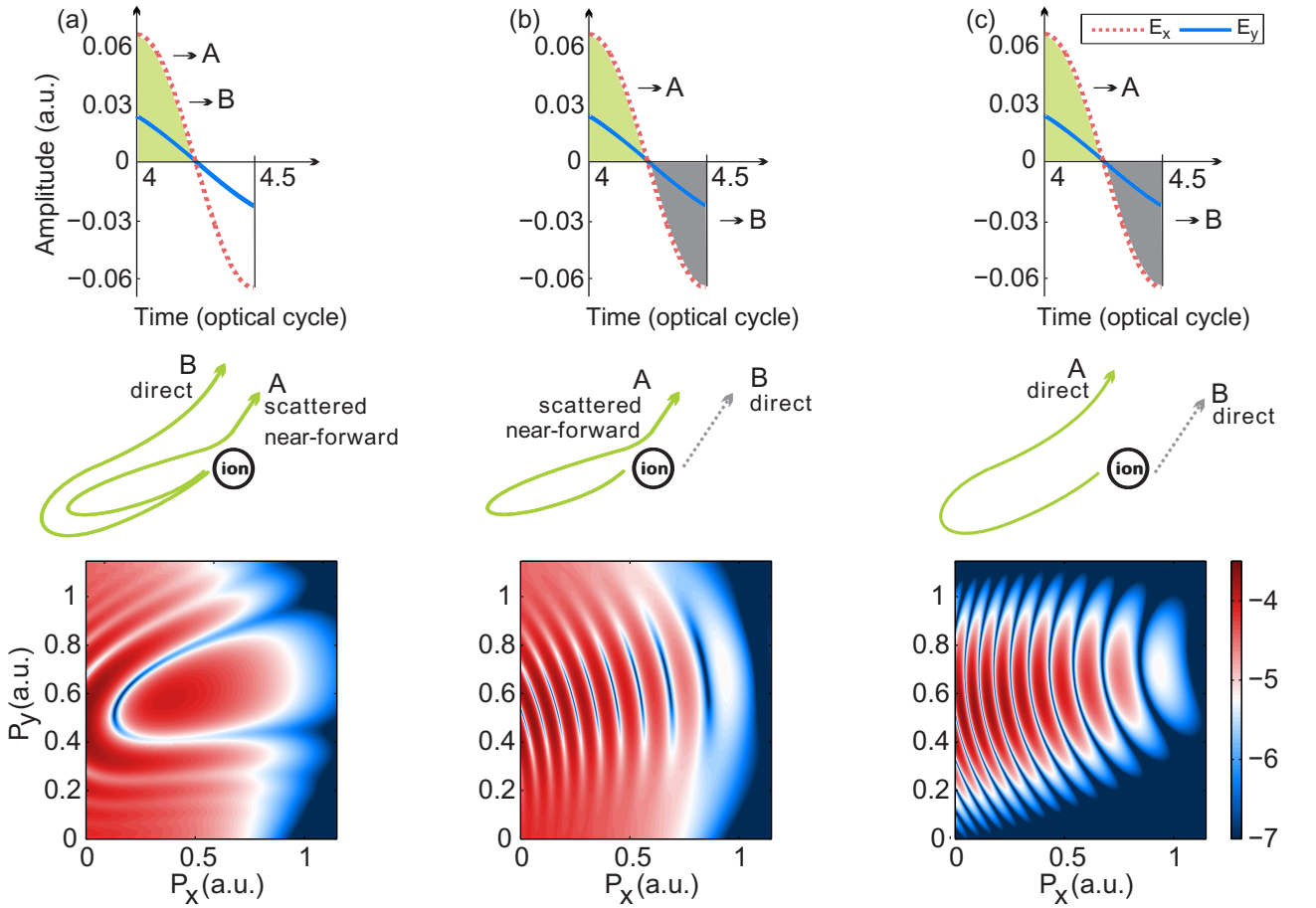

FIG. 3. Sketch for the three kinds of interferences marked as 1–3 in Fig. 2. The upper row presents the tunneling time of two electron wave packets A and B involved in the corresponding interference. The middle row shows the corresponding electron trajectories. The simulated interference structures with gSFA are shown in the bottom row.

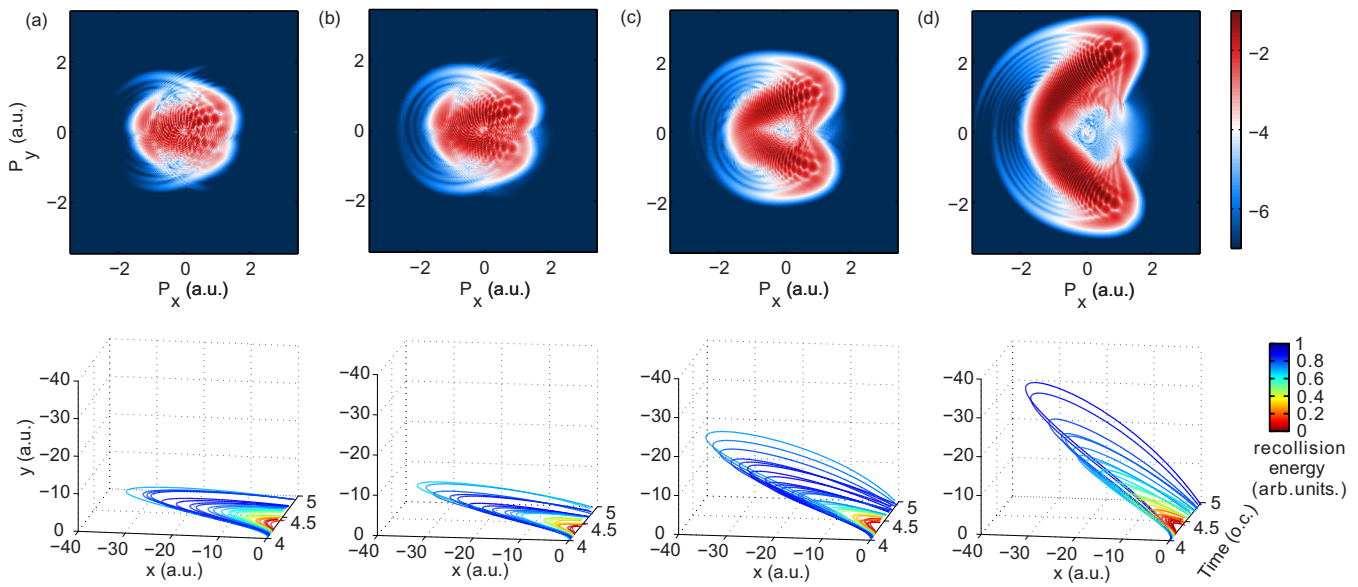

FIG. 4. Electron momentum distributions (upper row) and corresponding electron trajectories before scattering (bottom row). The intensity ratio $\varepsilon = I_y/I_x$ is (a) 1/36, (b) 1/16, (c) 1/4, and (d) 1. The relative phase $\phi = 0.25\pi$. In the bottom row, each color encodes a recollision energy, spanning from red to blue. Other laser parameters are the same as in Fig. 2.

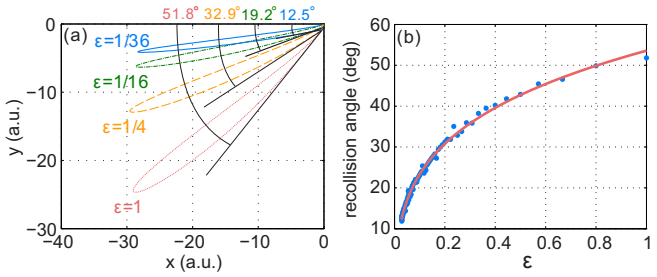

FIG. 5. (a) The most probable electron trajectories selected from the bottom row of Fig. 4. Trajectory and recollision angle are denoted in the same color with the corresponding relative intensity ratio. (b) The blue dots are the most probable recollision angles corresponding to the relative intensity ratio ε. The red curve represents a power function fit.

calculated using the classical model [47]. In our calculation, the ionization of the electrons is restricted within the temporal range $4.0T$–$4.25T$. We define the ionization axis [48] as the transient direction of the electric field at the instant t_i of tunneling. The electrons start their motions at an origin with initial transverse velocities $v_\perp$ uniformly distributed in $[-E_x/\omega, E_x/\omega]$ and perpendicular to the ionization axis. After the initial conditions are established, the trajectories of the electrons in the continuum are calculated by solving Newtonian equations with the Coulomb potential neglected. In the bottom row of Fig. 4, for each ε, a group of trajectories is selected. Colors of the trajectories encode the normalized recollision energies. One can find that the electron paths in OTC fields with bigger I_y have larger y components, leading to the bigger recollision angles.

In the above classical method, we assume the number of ionized electrons is the same for various instants of ionization and their initial velocities are equally distributed. Here the ionization probability will be taken into account to find the most probable recollision angles. The ionization probability obeys $\Gamma \sim \exp(-\frac{2(2I_p)^{3/2}}{3E(t_i)})\exp(-\frac{\sqrt{2I_p}}{E(t_i)}v_\perp^2)$ [49–51], where $E(t_i)$ is the transient electric field amplitude and $v_\perp$ is the initial transverse velocity. The weight of each electron trajectory is estimated corresponding to the ionization probability and thus the most probable electron trajectories for different ε are found, as presented in Fig. 5(a). The recollision angles of the most probable trajectories gradually increase in pace with the growth of ε, following the same trend with PMDs in Figs. 4(a)–4(d). For the case of $\varepsilon = 1$, where the two components have equal peak intensities, the recollision angle can reach as high as 51.8°. Furthermore, in Fig. 5(b), the most probable recollision angle as a function of the relative intensity is shown. One can find that the recollision angle grows continuously in the whole range. Thus by gradually altering the relative intensity, the structural information of the targets can be encoded in the hologram from the rescattering wave packet from different angles, implying that the SFPH using OTC fields can be a powerful tool to detect molecular structures.

IV. CONCLUSION

In summary, we have investigated SFPH in the OTC laser fields. Our TDSE calculations show that rich interference patterns appear in the momentum spectra of the photoelectrons and the origins of these interferences are identified with the gSFA method. By changing the relative phase of the OTC fields, we can switch on and off the holographic interference. This is based on the control of the revisit time of the returning electron wave packet. Additionally, we demonstrate that the recollision angle of the returning electron wave packet could be controlled via the relative intensity of the two fields.

SFPH is believed to be a potential tool in imaging the structure and ultrafast dynamics of atoms and molecules. To obtain full structural information of the molecular target, it is necessary to induce the electron to recollide the target from different angles. Thus, the temporal and spatial control of the recollision electron wave packet of SFPH demonstrated here will benefit the application of the SFPH.

ACKNOWLEDGMENT

This work was supported by the National Natural Science Foundation of China under Grants No. 61405064 and No. 11234004.

[1] W. Becker, F. Grasbon, R. Kopold, D. Milošević, G. Paulus, and H. Walther, Adv. At. Mol. Phys. **48**, 35 (2002).
[2] F. Krausz and M. Ivanov, Rev. Mod. Phys. **81**, 163 (2009).
[3] L. He, P. Lan, Q. Zhang, C. Zhai, F. Wang, W. Shi, and P. Lu, Phys. Rev. A **92**, 043403 (2015).
[4] Y. Li, P. Lan, H. Xie, M. He, X. Zhu, Q. Zhang, and P. Lu, Opt. Express **23**, 28801 (2015).
[5] Y. Zhou, C. Huang, Q. Liao, and P. Lu, Phys. Rev. Lett. **109**, 053004 (2012).
[6] A. Tong, Y. Zhou, and P. Lu, Opt. Express **23**, 15774 (2015); X. Ma, Y. Zhou, and P. Lu, Phys. Rev. A **93**, 013425 (2016).
[7] M. Li, P. Zhang, S. Luo, Y. Zhou, Q. Zhang, P. Lan, and P. Lu, Phys. Rev. A **92**, 063404 (2015).
[8] K. Liu, Q. Li, P. Lan, and P. Lu, Mol. Phys. **113**, 3247 (2015); Z. Wang, M. Li, Y. Zhou, Y. Li, P. Lan, and P. Lu, Phys. Rev. A **93**, 013418 (2016).
[9] P. Agostini, F. Fabre, G. Mainfray, G. Petite, and N. K. Rahman, Phys. Rev. Lett. **42**, 1127 (1979).
[10] F. Lindner, M. G. Schätzel, H. Walther, A. Baltuška, E. Goulielmakis, F. Krausz, D. B. Milošević, D. Bauer, W. Becker, and G. G. Paulus, Phys. Rev. Lett. **95**, 040401 (2005).
[11] D. G. Arbó, E. Persson, and J. Burgdörfer, Phys. Rev. A **74**, 063407 (2006).
[12] D. G. Arbó, K. L. Ishikawa, K. Schiessl, E. Persson, and J. Burgdörfer, Phys. Rev. A **82**, 043426 (2010).
[13] X. Xie, S. Roither, D. Kartashov, E. Persson, D. G. Arbó, L. Zhang, S. Gräfe, M. S. Schöffler, J. Burgdörfer, A. Baltuška, and M. Kitzler, Phys. Rev. Lett. **108**, 193004 (2012).
[14] P. B. Corkum, Phys. Rev. Lett. **71**, 1994 (1993).
[15] Y. Huismans, A. Rouzée, A. Gijsbertsen, J. Jungmann, A. Smolkowska, P. Logman, F. Lépine, C. Cauchy, S. Zamith, T. Marchenko, J. Bakker, G. Berden, B. Redlich, A. van der Meer,

H. Muller, W. Vermin, K. Schafer, M. Spanner, M. Ivanov, O. Smirnova, D. Bauer, S. Popruzhenko, and M. Vrakking, Science **331**, 61 (2011).
[16] X.-B. Bian, Y. Huismans, O. Smirnova, Kai-Jun Yuan, M. J. J. Vrakking, and A. D. Bandrauk, Phys. Rev. A **84**, 043420 (2011).
[17] D. Gabor, Nature (London) **161**, 777 (1948).
[18] D. D. Hickstein, P. Ranitovic, S. Witte, X.-M. Tong, Y. Huismans, P. Arpin, X. Zhou, K. E. Keister, C. W. Hogle, B. Zhang, C. Ding, P. Johnsson, N. Toshima, M. J. J. Vrakking, M. M. Murnane, and H. C. Kapteyn, Phys. Rev. Lett. **109**, 073004 (2012).
[19] M. Meckel, A. Staudte, S. Patchkovskii, D. M. Villeneuve, P. B. Corkum, R. Dörner, and M. Spanner, Nat. Phys. **10**, 594 (2014).
[20] D. G. Arbó, C. Lemell, S. Nagele, N. Camus, L. Fechner, A. Krupp, T. Pfeifer, S. D. López, R. Moshammer, and J. Burgdörfer, Phys. Rev. A **92**, 023402 (2015).
[21] Y. Zhou, O. I. Tolstikhin, and T. Morishita, Near-forward rescattering photoelectron holography in strong-field ionization: Extraction of the phase of the scattering (unpublished).
[22] M. Kitzler and M. Lezius, Phys. Rev. Lett. **95**, 253001 (2005).
[23] G. Lambert, B. Vodungbo, J. Gautier, B. Mahieu, V. Malka, S. Sebban, P. Zeitoun, J. Luning, J. Perron, A. Andreev, S. Stremoukhov, F. Ardana-Lamas, A. Dax, C. P. Hauri, A. Sardinha, and M. Fajardo, Nat. Commun. **6**, 6167 (2015).
[24] L. Brugnera, D. J. Hoffmann, T. Siegel, F. Frank, A. Zaïr, J. W. G. Tisch, and J. P. Marangos, Phys. Rev. Lett. **107**, 153902 (2011).
[25] D. Shafir, H. Soifer, B. D. Bruner, M. Dagan, Y. Mairesse, S. Patchkovskii, M. Ivanov, O. Smirnova, and Nirit Dudovich, Nature (London) **485**, 343 (2012).
[26] J. Zhao and M. Lein, Phys. Rev. Lett. **111**, 043901 (2013).
[27] D. Shafir, Y. Mairesse, D. M. Villeneuve, P. B. Corkum, and N. Dudovich, Nat. Phys. **5**, 412 (2009).
[28] H. Niikura, H. J. Wörner, D. M. Villeneuve, and P. B. Corkum, Phys. Rev. Lett. **107**, 093004 (2011).
[29] Y. Zhou, C. Huang, A. Tong, Q. Liao, and P. Lu, Opt. Express **19**, 2301 (2011).
[30] Y. Zhou, C. Huang, Q. Liao, W. Hong, and P. Lu, Opt. Lett. **36**, 2758 (2011).
[31] L. Zhang, X. Xie, S. Roither, Y. Zhou, P. Lu, D. Kartashov, M. Schöffler, D. Shafir, P. B. Corkum, A. Baltuška, A. Staudte, and M. Kitzler, Phys. Rev. Lett. **112**, 193002 (2014).
[32] M. Richter, M. Kunitski, M. Schöffler, T. Jahnke, L. P. H. Schmidt, M. Li, Y. Liu, and R. Dörner, Phys. Rev. Lett. **114**, 143001 (2015).
[33] X. Xie, Phys. Rev. Lett. **114**, 173003 (2015).
[34] M. Li, J.-W. Geng, M.-M. Liu, X. Zheng, L.-Y. Peng, Q. Gong, and Y. Liu, Phys. Rev. A **92**, 013416 (2015).
[35] M. D. Feit, J. A. Fleck, Jr., and A. Steiger, J. Comput. Phys. **47**, 412 (1982).
[36] M. Protopapas, C. H. Keitel, and P. L. Knight, Rep. Prog. Phys. **60**, 389 (1997).
[37] X. M. Tong, K. Hino, and N. Toshima, Phys. Rev. A **74**, 031405(R) (2006).
[38] S. Chelkowski, C. Foisy, and A. D. Bandrauk, Phys. Rev. A **57**, 1176 (1998).
[39] X. M. Tong, S. Watahiki, K. Hino, and N. Toshima, Phys. Rev. Lett. **99**, 093001 (2007).
[40] P. L. He, N. Takemoto, and F. He, Phys. Rev. A **91**, 063413 (2015).
[41] Y. Huismans, A. Gijsbertsen, A. S. Smolkowska, J. H. Jungmann, A. Rouzée, P. S. W. M. Logman, F. Lépine, C. Cauchy, S. Zamith, T. Marchenko, J. M. Bakker, G. Berden, B. Redlich, A. F. G. van der Meer, M. Y. Ivanov, T.-M. Yan, D. Bauer, O. Smirnova, and M. J. J. Vrakking, Phys. Rev. Lett. **109**, 013002 (2012).
[42] D. B. Milošević and W. Becker, Phys. Rev. A **66**, 063417 (2002).
[43] D. B. Milošević, G. G. Paulus, D. Bauer, and W. Becker, J. Phys. B: At., Mol. Opt. Phys. **39**, R203 (2006).
[44] P. Salières, B. Carré, L. Le Déroff, F. Grasbon, G. G. Paulus, H. Walther, R. Kopold, W. Becker, D. B. Milošević, A. Sanpera, and M. Lewenstein, Science **292**, 902 (2001).
[45] C. C. Chirilč, I. Dreissigacker, E. V. van der Zwan, and M. Lein, Phys. Rev. A **81**, 033412 (2010).
[46] Y. Li, X. Zhu, Q. Zhang, M. Qin, and P. Lu, Opt. Express **21**, 4896 (2013).
[47] W. Becker, X. Liu, P. Jo Ho, and J. H. Eberly, Rev. Mod. Phys. **84**, 1011 (2012).
[48] D. Shafir, Y. Mairesse, H. J. Wörner, K. Rupnik, D. M. Villeneuve, P. B. Corkum, and N. Dudovich, New J. Phys. **12**, 073032 (2010).
[49] L. Arissian, C. Smeenk, F. Turner, C. Trallero, A. V. Sokolov, D. M. Villeneuve, A. Staudte, and P. B. Corkum, Phys. Rev. Lett. **105**, 133002 (2010).
[50] M. Ivanov, M. Spanner, and O. Smirnova, J. Mod. Opt. **52**, 165 (2005).
[51] D. I. Bondar, Phys. Rev. A **78**, 015405 (2008).